

ILIT:
A PREDICTIVE LIGHT TRANSPORT MODEL
FOR THE HUMAN IRIS

by

Michael Wing Young Lam

A thesis
presented to the University of Waterloo
in fulfilment of the
thesis requirement for the degree of
Master of Mathematics
in
Computer Science

Waterloo, Ontario, Canada, 2006
© Michael Wing Young Lam 2006

I hereby declare that I am the sole author of this thesis.

I authorize the University of Waterloo to lend this thesis to other institutions or individuals for the purpose of scholarly research.

I further authorize the University of Waterloo to reproduce this thesis by photocopying or by other means, in total or in part, at the request of other institutions or individuals for the purpose of scholarly research.

Abstract

Recently, light interactions with organic matter have become the object of detailed investigations by image synthesis researchers. Besides allowing these materials to be rendered in a more intuitive manner, these efforts aim to extend the scope of computer graphics applications to areas such as applied optics and biomedical imaging. There are, however, organic materials that still lack predictive simulation solutions. Among these, the ocular tissues, especially those forming the human iris, pose the most challenging modeling problems which are often associated with data scarcity. In this thesis, we describe the first biophysically-based light transport model for the human iris ever presented in the scientific literature. The proposed model algorithmically simulates the light scattering and absorption processes occurring within the iridal tissues, and computes the spectral radiometric responses of these tissues. Its design is based on the current scientific understanding of the iridal morphological and optical characteristics, and it is controlled by parameters directly related to these biophysical attributes. The accuracy and predictability of the spectral results provided by the model are evaluated through comparisons with actual measured iridal data, and its integration into rendering frameworks is illustrated through the generation of images depicting iridal chromatic variations.

Acknowledgments

I am deeply indebted to my advisor and my best critic, Dr. Gladimir Baranoski, for his selfless help and support throughout the research, including many reviews of the thesis and countless circumventions of his personal schedules in order for us to hold meetings. I have also benefited tremendously from his relentless pursuit of honest and scientifically correct way to computer graphics.

I am grateful to Dr. Francisco Imai of Rochester Institute of Technology for his permission to use the measured iridal data from his research, which makes the quantitative comparison possible. I also would like to thank Aravind Krishnaswamy, who provided invaluable directions to the difficult-to-find data of melanin pigments.

Very special thanks go to Mrs. Adriane Baranoski and Ms. Kathy Chan for their patience and help as models for the often painful iris photography sessions.

Finally I wish to express my sincerest gratitude to Dr. Bruce Simpson and Dr. Jeff Orchard, for finding my research interesting and for spending their valuable time on reviewing the thesis.

Dedication

This thesis is dedicated to the loving memory of my grandmother, Mrs. Chung Yuk Lam (1913-2004). Thank you for everything.

Contents

1	Introduction	1
1.1	Previous Related Work	2
1.2	Thesis Contribution	4
1.3	Thesis Organization	5
2	Biophysical Background	7
2.1	Overview of Ocular Tissues	7
2.2	Iris: Morphology and Optics	9
2.2.1	Absorption Phenomenon	10
2.2.2	Scattering Phenomenon	11
3	The ILIT Model	13
3.1	Reflection and Refraction at the Interfaces	15
3.2	Diffuse Perturbation	15
3.3	Absorption	19
3.4	Attenuation and Scattering	20
4	Evaluation Issues	23
4.1	Procedures	23
4.2	Data	24

5	Results and Discussion	29
5.1	Quantitative Predictions	29
5.2	Qualitative Predictions	31
5.3	Rendering Performance	36
6	Conclusion and Future Work	39

List of Tables

3.1	Random numbers used in the simulations.	14
4.1	Refractive indices used in the simulations.	26
4.2	Melanin concentrations (<i>mg/ml</i>) used in the simulations.	27
6.1	Per-iris amount of pigments (μg).	64

List of Figures

1.1	An iridal image rendered using the proposed model and framed by an artist's conception of the human eye.	2
2.1	Sketch showing the visible ocular tissues and a zoom in of the iridal layers.	8
2.2	Spectral molar absorption (extinction) coefficient curves for natural pigments (chromophores) present in the iridal tissues. Top: melanins [Jacques 2001]. Bottom left: hemoglobins [Prahl 1999]. Bottom right: carotenoids [Zscheile <i>et al.</i> 1942].	12
3.1	Diagram illustrating possible paths (A, B, C and D) that can be followed by rays traversing the iridal tissues. The semi-circles represent diffuse perturbation, the double circles represent Rayleigh scattering (forward or backward), and the stars represent absorption events. .	15
3.2	Rejection sampling for reflected ray. Top: $\vec{v}_d \cdot \vec{n} > 0$, ray accepted. Bottom: $\vec{v}_d \cdot \vec{n} < 0$, ray rejected (requires new sample).	17
3.3	Rejection sampling for transmitted ray. Top: $\vec{v}_d \cdot \vec{n} < 0$, ray accepted. Bottom: $\vec{v}_d \cdot \vec{n} > 0$, ray rejected (requires new sample).	18
3.4	Flowcharts illustrating the algorithms used by the ILIT model to simulate light transport in the ABL (left) and Stromal Layer (right). .	20
5.1	Comparison of modeled reflected radiance curves provided by the ILIT model with actual reflected radiance curves measured by Imai [2000] and Unander [2000]. Top: heavily pigmented iris specimen. Bottom left: moderately pigmented specimen. Bottom right: lightly pigmented specimen. The error bars indicate maximum and minimum values observed in the actual measurements.	30

5.2	Comparison of modeled reflectance curves provided by the ILIT model considering specimens with different levels of pigmentation: low (L) and high (H).	32
5.3	Comparison of modeled reflectance curves provided by the ILIT model considering different melanin distributions between the ABL and the Stromal Layer (expressed in terms of the percentage of melanin presented in the ABL).	33
5.4	Modeled iridal BRDFs measured at $550nm$. Left: considering an angle of incidence of 0° . Right: considering an angle of incidence of 60° . Plots correspond to scattering profiles taken at the principal plane of incidence, and considering specimens with different levels of of pigmentation, namely low (L) and high (H).	34
5.5	Images showing iridal chromatic variations obtained using the ILIT model. From left to right, the iridal eumelanin concentration was decreased from $1.008mg/ml$ to $0.1201mg/ml$, and the iridal pheomelanin concentration from $0.2674mg/ml$ to $0.0194mg/ml$. From top to bottom, the percentage of melanin presented in the ABL was altered: 20% (top row), 50% (middle row) and 80% (bottom row). . .	35
5.6	Images showing iridal chromatic variations of a lightly pigmented iris (eumelanin concentration: $0.1201mg/ml$, pheomelanin concentration: $0.0194mg/ml$) obtained by varying the thickness of the ABL and the Stromal Layer. From left to right: Iris thickness is decreased by 0%, 5%, 15%, 30% and 50%. From top to bottom, the percentage of melanin presented in the ABL was altered: 20% (top row), 50% (middle row) and 80% (bottom row).	36
5.7	Images showing iridal chromatic variations of a lightly pigmented iris (eumelanin concentration: $0.1201mg/ml$) obtained by increasing the pheomelanin concentration. (From left to right) Top: pheomelanin concentrations of $0.0388mg/ml$, $0.1164mg/ml$, $0.194mg/ml$. Bottom: $0.2716mg/ml$, $0.3492mg/ml$, $0.4268mg/ml$	37
6.1	Images showing iridal chromatic variations obtained by varying the chromaticity coordinates. From left to right: (eumelanin concentration, pheomelanin concentration, ABL melanin portion) selected to be ($1.008mg/ml$, $0.2674mg/ml$, 80%), ($0.4674mg/ml$, $0.1124mg/ml$, 50%), and ($0.1201mg/ml$, $0.0194mg/ml$, 20%) respectively. Top: using selected CIE-1931 chromaticity coordinates. Bottom: using SMPTE chromaticity coordinates.	67

Table of Symbols

u_i	Uniformly distributed random number in the interval $[0, 1]$	14
F	Fresnel coefficient	15
α_d	Polar angle of a diffuse perturbation	16
β_d	Azimuthal angle of a diffuse perturbation	16
\vec{v}_d	Diffusely propagated ray	16
\vec{v}_r	Reflected ray	16
\vec{n}	Normal vector	16
\vec{v}_t	Transmitted ray	16
Δp	Distance travelled by a photon in a medium	19
λ	Wavelength	19
μ_a	Absorption coefficient	19
θ	Angle between ray direction and medium normal	19
μ_{aA}	Absorption coefficient of the ABL	19
μ	Attenuation coefficient	20
μ_{aS}	Absorption coefficient of the Stromal Layer	20
r	Collagen fibril radius	21
f_{col}	Volume fraction of collagen	21
η	Refractive index	21
μ_s	Scattering coefficient	21
η_{col}	Refractive index of Type I collagen	21
η_{base}	Refractive index of optical base material	21
h_S	Thickness of the Stromal Layer	22
P_μ	Attenuation probability	22
α_R	Polar angle of a Rayleigh perturbation	22
β_R	Azimuthal angle of a Rayleigh perturbation	22
η_{tear}	Refractive index of human tear	24
η_{cor}	Refractive index of human cornea	24
η_{ah}	Refractive index of human aqueous humor	24
η_A	Weighted refractive index	25

η_{fib}	Refractive index of fibroblast	25
f_{fib}	Volume fraction of ABL fibroblast	25
f_{col}	Volume fraction of Stromal Layer collagen	25
η_{air}	Refractive index of air	26
$d\omega_i$	Differential solid angle	59
L_i	Incident radiance	59
L_r	Reflected radiance	59
f_r	BRDF	59
$d\omega$	Differential solid angle	59
(θ, ϕ)	Spherical coordinates of a sphere of unit radius	59
ρ	Reflectance	60
dL_r	Differential reflected radiance	60
m_e	Iridal eumelanin mass	64
m_p	Iridal pheomelanin mass	64
m_l	Iridal lutein mass	64
m_z	Iridal zeaxanthin mass	64

Chapter 1

Introduction

The realistic rendering of human features has always been a challenge for the computer graphics community. Although it is still true that the closer a rendered face resembles that of a real human, the more critical is our perception of it [93], notable progress has been achieved in the generation of believable images of virtual humans. Consequently, it is natural that we as researchers attempt to go a step further by looking for modeling solutions that can also lead to predictable images [32, 70]. Although these solutions usually require more resources and time to be developed and properly evaluated using actual measured data, they can make the image synthesis process more automatic and facilitate the reproduction of realistic results. Furthermore, a predictive modeling approach has a broad scope of scientific applications. Despite recent multidisciplinary efforts in this area, however, there are still human features for which predictive rendering solutions are either scarce or nonexistent. In this thesis, we investigate one of these features, namely the human iris (Figure 1.1), arguably the most striking ocular structure affecting facial



Figure 1.1: An iridal image rendered using the proposed model and framed by an artist’s conception of the human eye.

appearance. Appropriately, it takes its name from $\iota\rho\iota\varsigma$, the Greek goddess of the rainbow [43, 96].

1.1 Previous Related Work

The human iris is a complex optical system, and its characteristic spectral signature is represented by chromatic attributes (*e.g.*, hue and saturation [102]) which are among the most readily discernible traits of the human phenotype [97]. These attributes are associated with the spectral light distribution of the iridal tissues, and researchers from different fields have been studying the photobiological properties of these tissues for decades. In colorimetry¹, the investigations are oriented towards the measuring and classification of iridal chromatic attributes [57, 75, 82, 41], and the study of their dependence [40] on the distribution and content of iridal chromophores (pigments) [43] and ocular drugs [30]. In computer vision, researchers use

¹The study of colour measurement [40].

iridal chromaticity (specified by the dominant wavelength and purity of the iridal colour [102]) in estimations of environmental illumination [91]. In the medical field, the research efforts are focused on the relationship between iridal pigmentation and the incidence of several eye diseases such as the degeneration of ocular tissues [79, 39, 16] and melanoma [2, 95, 71]. In biophysics and investigative ophthalmology, researchers examine the relationship between iridal chromatic attributes and phenomena such as the pupil size and pupillary light reflex [6, 99]. It is worth noting that, although mechanical [101] and computational models [19, 35, 36, 68, 89] have been proposed in the biomedical literature to investigate the processes that control the amount of light that enters the human eye, these models are aimed at the light interactions with ocular fundus tissues such as the retina. The processes of light propagation and absorption within the iridal tissues are outside the scope of these models. Incidentally, the human iris is also object of investigation in biometrics due to the uniqueness of its texture patterns (the probability of two irides agreeing is about one in seven billion [14]), which can be used in identification methodologies [9, 61, 96].

In the computer graphics literature, few papers related to the human eye’s appearance have been published to date. In their research aimed at ocular surgical simulations, Sagar *et al.* [73] used a Gouraud shaded polygon with colours specified by a colour ramp to represent the human iris. Halstead *et al.* [34] proposed an algorithm for the reconstruction of curved surfaces from specular reflection patterns that can be applied on the measurement of the outermost ocular tissue, namely the human cornea. Lefohn *et al.* [50] presented the first biologically motivated algorithm specifically designed for the rendering of realistic looking irides. Their

modeling approach is based on an ocular prosthetics methodology. According to Lefohn *et al.* [50], the development of a biophysically-based procedural solution for the rendering of the human iris would have to overcome obstacles associated with the inherent complexity of the iridal tissues and data scarcity. Despite the fact that the biophysical processes of light interaction with these tissues have not been simulated by Lefohn *et al.* [50], it is important to note that their modeling approach includes the geometrical attributes of the human iris, and it can produce believable images of the human eye. Also aiming at iridal image synthesis, but using an image processing paradigm, Wecker *et al.* [94] proposed a technique to decompose iridal images into several components. These are then recombined to generate a new image. Recently, Deering [15] presented an algorithm to model ocular photoreceptor cells, and carefully examined visual perception issues. Although his work was not aimed at the rendering of the human iris, it further expanded the biophysical foundation for eye-related research in computer graphics.

1.2 Thesis Contribution

In this thesis, we propose a novel predictive light transport model for the human iris. Our investigation is aimed at computer graphics and tissue optics applications, and it focus on light-matter interaction issues, *i.e.*, morphogenetic issues responsible for the distinctiveness of the iridal texture patterns are beyond the scope of this work. The proposed iridal light transport model, henceforth referred to as the ILIT model, takes into account the mechanisms of light propagation and absorption in the iridal tissues, and it is controlled by biophysically meaningful parameters.

The ILIT model is implemented using Monte Carlo techniques [37, 66], whose applicability to the development or testing of models of light interaction with human tissues has been verified by biomedical scientists [98, 92, 67, 84] and computer graphics researchers [38, 62, 78, 53, 48, 21]. Its accuracy and predictability are evaluated through comparisons of modeled results with actual measured iridal data, as well as observations of actual phenomena reported in the scientific literature. The complete biophysical data set used in our evaluation experiments is provided so that they can be seamlessly reproduced by computer graphics and biomedical researchers. We also present images of human irides rendered using the ILIT model to illustrate its qualitative capabilities and its potential use in image synthesis pipelines.

1.3 Thesis Organization

The remainder of this thesis is organized as follows. The next chapter, *Biophysical Background*, provides a concise overview of the human eye, and a more detailed description of the iris with an emphasis on factors affecting the light interaction with iridal tissues. Chapter 3, *The ILIT Model*, presents the ILIT model. Chapter 4, *Evaluation Issues*, outlines our evaluation approach and provides the biophysical data set used in our simulations. Chapter 5, *Results and Discussion*, presents the results of the quantitative and qualitative experiments used to evaluate the accuracy and predictability of the ILIT model, as well as iridal images obtained by integrating it into a standard rendering framework. The thesis closes with a summary and directions for future work.

Chapter 2

Biophysical Background

In this chapter, we briefly examine the visible ocular tissues, and define the biophysical terms used throughout this thesis. We also present qualitative and quantitative biophysical information used in the design of the ILIT model. The reader interested in a more comprehensive description of the ocular anatomy and physiology is referred to classical books on these topics [26, 51, 60, 77].

2.1 Overview of Ocular Tissues

The shape of the human eyeball can be approximated by two incompletely overlapping spheres with different radii, with the smaller sphere positioned in the front of the face. Its appearance is mostly determined by the interaction of light with five ocular media illustrated in Figure 2.1, namely cornea, sclera, lens, aqueous humor and iris.

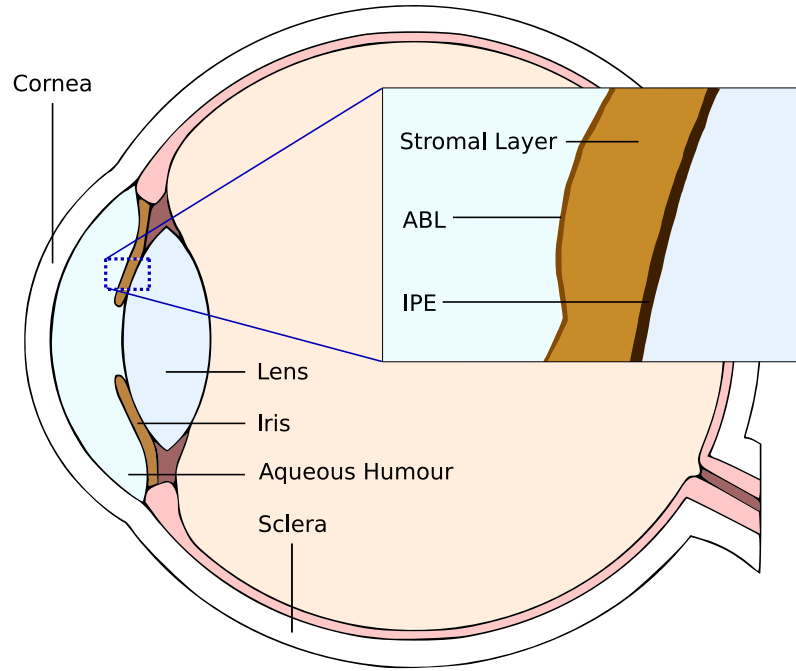


Figure 2.1: Sketch showing the visible ocular tissues and a zoom in of the iridal layers.

The sclera contains the “white” part of the visible eyeball, and the cornea is a clear tissue, serving as its only entrance of light. In its normal state, the cornea appears transparent, and it is covered by a tear film that makes its surface optically smooth [34]. The space between the cornea and the lens, a colourless tissue [8], is occupied by the aqueous humor, a clear alkaline liquid. Although measurements of cornea and aqueous humor transmittance [8, 4, 88, 27] suggest a slight wavelength dependence, it is important to note that such measurements did not include backscattered light which may also affect the spectral signature of these media.

The iris is a thin pigmented diaphragm stretching across the front of the eye and surrounding the pupil. Due to the support of the neighboring lens, it has a cone-like

shape pointing towards the front of the eye. It can be described as a multilayered tissue (Figure 2.1), and its spectral signature is determined by its morphological and optical characteristics, which are concisely described in the following section.

2.2 Iris: Morphology and Optics

The outermost iridal layer is the ABL (Anterior Border Layer). It consists of a dense arrangement of pigmented cells, collagen fibers and fibroblasts [23, 60, 77]. Immediately behind the ABL, we find the Stromal Layer. Although both layers consist of connective tissue and pigmented cells, the Stromal Layer is less dense than the ABL [23]. The Stromal Layer is also characterized by the presence of loosely arranged collagen fibrils. The innermost layer is an opaque tissue called IPE (Iris Pigment Epithelium). It consists of heavily pigmented epithelial cells which are tightly fused by intercellular connections [43].

The primary factors affecting the iridal chromatic attributes are the density and pigmentation of the iridal tissues [43]. Most of the chromatic variations observed in the human iris are due to absorption caused by iridal pigmentation, specially that of the ABL [43, 96]. However, as pointed out by Delori *et al.* [16], instead of a simple continuum with pigment content, there are discrete families of spectral signatures which cannot be predicted by a simple absorption model. When there is little pigmentation in the ABL, the iridal spectra is dominated by tissue scattering [16], *i.e.*, light is scattered by stromal collagen fibrils.

2.2.1 Absorption Phenomenon

The absorption spectra of the pigment present in the iridal tissues are shown in Figure 2.2. Among the iridal pigments, the melanin provides the most significant qualitative and quantitative contributions to the variations in the iridal chromatic attributes, which are directly affected by the total content and distribution of this pigment in the ABL and the Stromal Layer [59, 42]. The heavily pigmented IPE provides only a background tint [42, 43]. It plays a minor role on iridal colour since it reflects only a small portion of the incident light, and its pigmentation does not present a detectable variance between irides of different colours [23].

Two types of melanin are present in the human iris: the brown-black eumelanin and the red-yellow pheomelanin. The former is found in larger concentrations than the latter [58]. Experiments by Prota *et al.* [69] indicate that lightly pigmented irides show a low content of both pigments, while heavily pigmented irides exhibit a high content. The irides showing a green hue in the region near the pupil, known as the pupillary zone [73], and a blue hue on the peripheral region, known as the ciliary zone [73], proved to be eumelanic, whereas irides exhibiting a brown hue near the pupil and a green hue on the periphery are described as featuring pheomelanic or a mixed type pigmentation [69]. Wistrand *et al.* [100] also pointed out that irides with mixed hues usually have higher melanin concentration in the pupillary zone, and in the bottom of iridal depressions called crypts [73].

Besides the melanins, other natural pigments, notably the hemoglobins and the carotenoids, may contribute to the iridal spectral characteristics of healthy human eyes. The two types of hemoglobins (oxygenated and deoxygenated) are found

in the stromal blood vessels [26]. Similarly, two types of carotenoids (lutein and zeaxanthin) are also found in the Stromal Layer [7]. It has been suggested that a pigment called lipofuscin [83] may also contribute to iridal chromatic variations [50]. However, to the best of our knowledge, quantitative evidence to fully support this hypothesis for healthy human irides has not become available in the biomedical literature to date. Its occurrence in the human eye is usually associated with age-related degeneration of ocular fundus tissues [18, 17, 29].

2.2.2 Scattering Phenomenon

The scattering caused by the stromal collagen fibrils occurs in a Rayleigh fashion [97] which is proportional to the forth power of the light frequency [80, 81]. Hence, it may produce grey or blue hues since shorter wavelengths are preferentially attenuated [16, 97, 96]. As light gets scattered multiple times inside the iridal layers, its spatial distribution quickly becomes diffuse. As a result, the iridal surface scattering distribution has a near-Lambertian profile [10, 96]. Thus, different combinations of the absorption and scattering effects can create a continuum of iridal colours from dark brown (more absorption) to light blue (more scattering).

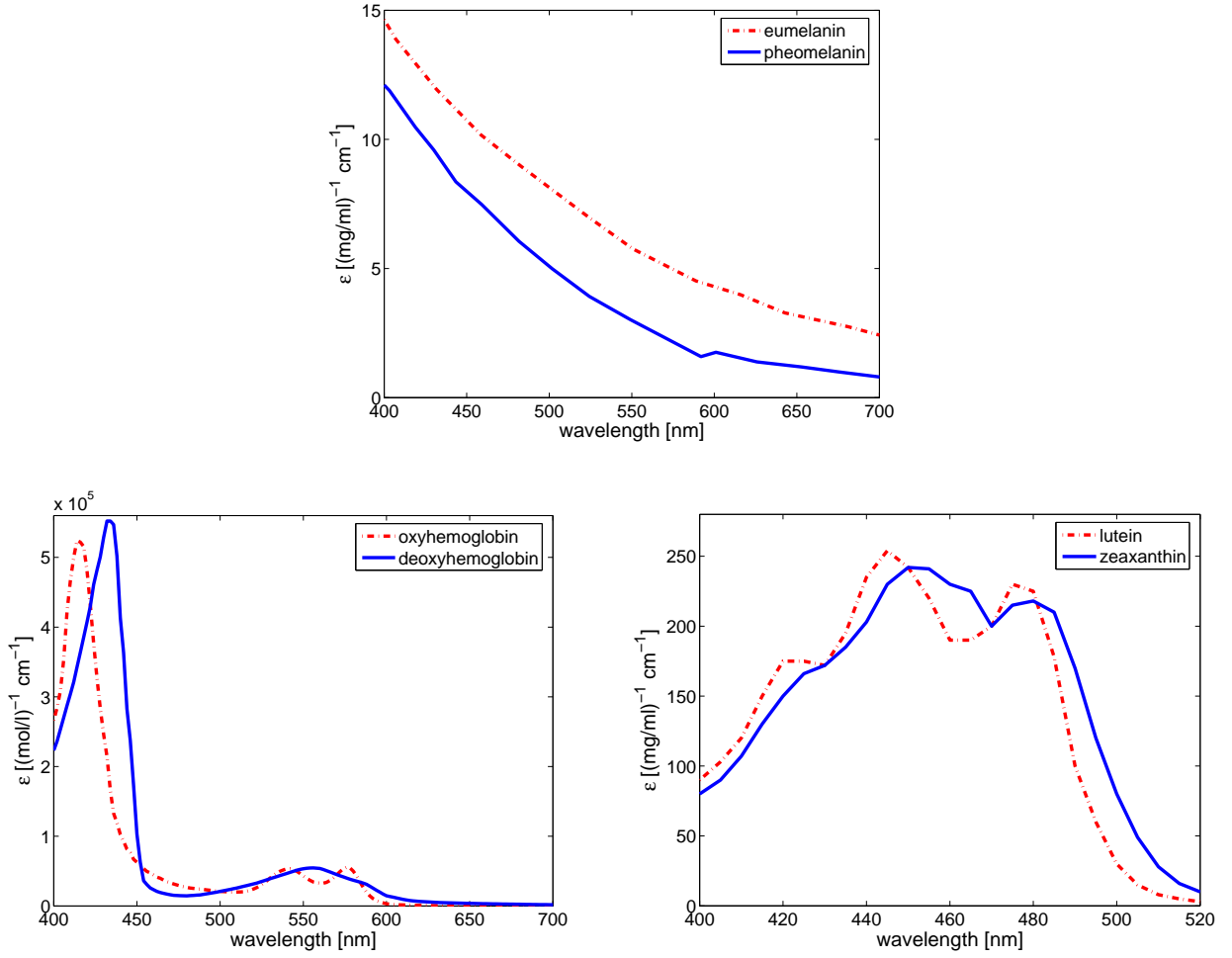


Figure 2.2: Spectral molar absorption (extinction) coefficient curves for natural pigments (chromophores) present in the iridal tissues. Top: melanins [Jacques 2001]. Bottom left: hemoglobins [Prahl 1999]. Bottom right: carotenoids [Zscheile *et al.* 1942].

Chapter 3

The ILIT Model

The proposed model has an algorithmic formulation in which light is represented by discrete rays, each one associated with a wavelength. Although geometrical optics is used in the light transport simulations performed by the model, wave optics approximations are employed where appropriate (*e.g.*, the computation of the optical free path length for a given ray traversing the iridal tissues at a given wavelength). The ILIT model simulates light interaction with human iris through a stochastic process whose states are represented by the interface between the iris and the surrounding medium, and the interfaces between adjacent iridal tissues, namely ABL, Stromal Layer and IPE. It is assumed that light transmitted to the IPE is absorbed within this tissue (Section 2.2).

A ray that traverses from one iridal layer to the next must pass the interface between these layers. At these interfaces the rays can be reflected or refracted. The results of these interactions are associated with the transition probabilities of the

stochastic process, *i.e.*, they determine the next layer that the ray will traverse, thus its next state. Scattering events affecting the ray direction of propagation may also prompt the transition from one state to another. Absorption events are associated with the termination probabilities of the stochastic process, *i.e.*, when a ray is absorbed its transport simulation is halted.

Figure 3.1 illustrates possible paths that can be followed by a ray traversing the iridal tissues as well as the occurrence of scattering and absorption events. The non-deterministic simulation of these events employs random numbers u_i , for $i = 1, 2, \dots, 9$, uniformly distributed in the interval $[0, 1]$, which are generated on the fly during the simulations. The following table summarizes all the u_i used in the model, which will be further explained in the next sections.

Table 3.1: Random numbers used in the simulations.

Symbol	Usage
u_1	Fresnel interaction
u_2	Diffuse perturbation, polar angle
u_3	Diffuse perturbation, azimuthal angle
u_4	Absorption test
u_5	Attenuation test
u_6	Attenuation type
u_7	Rayleigh scattering perturbation, polar angle
u_8	Rayleigh scattering perturbation, rejection sampling
u_9	Rayleigh scattering perturbation, azimuthal angle

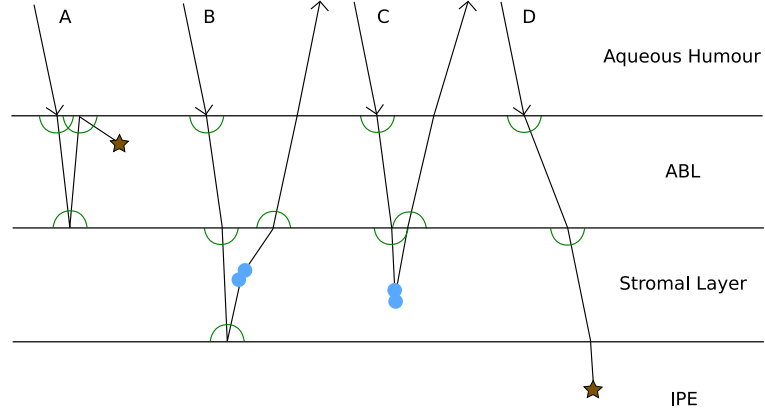


Figure 3.1: Diagram illustrating possible paths (A, B, C and D) that can be followed by rays traversing the iridal tissues. The semi-circles represent diffuse perturbation, the double circles represent Rayleigh scattering (forward or backward), and the stars represent absorption events.

3.1 Reflection and Refraction at the Interfaces

Since each layer is simulated with its unique refractive index, either reflection or refraction occurs at all the interfaces. The ILIT model simulates these interactions by computing the Fresnel coefficient (F) associated with the incoming ray, and taking into account the refractive index differences of the media. If $u_1 \leq F$, then the ray is reflected. Otherwise, it is refracted. The Fresnel coefficients are computed through the Fresnel equations [40, 76].

3.2 Diffuse Perturbation

When a ray enters either the ABL or the Stromal Layer (Figure 3.4), it is diffusively perturbed due to the internal arrangement of the tissues (Section 2.2). In order to account for this effect, the ILIT model uses a warping function based on a cosine

distribution [76]. According to this function, the polar (α_d) and azimuthal (β_d) angles of the diffusively propagated rays, \vec{v}_d , are given by:

$$(\alpha_d, \beta_d) = (\arccos((1 - u_2)^{\frac{1}{2}}), 2\pi u_3). \quad (3.1)$$

Rejection sampling is used to prevent that the perturbed direction of propagation invalidates the result of the Fresnel test performed at the previous interface. For example, if the test results in a reflected ray, \vec{v}_r , then rejection sampling is used to guarantee that $\vec{v}_d \cdot \vec{n} > 0$, where \vec{n} corresponds to specimens' normal vector (Figure 3.2).

Similarly, if the test results in a transmitted ray, \vec{v}_t , rejection sampling is used to guarantee that $\vec{v}_d \cdot \vec{n} < 0$ (Figure 3.3).

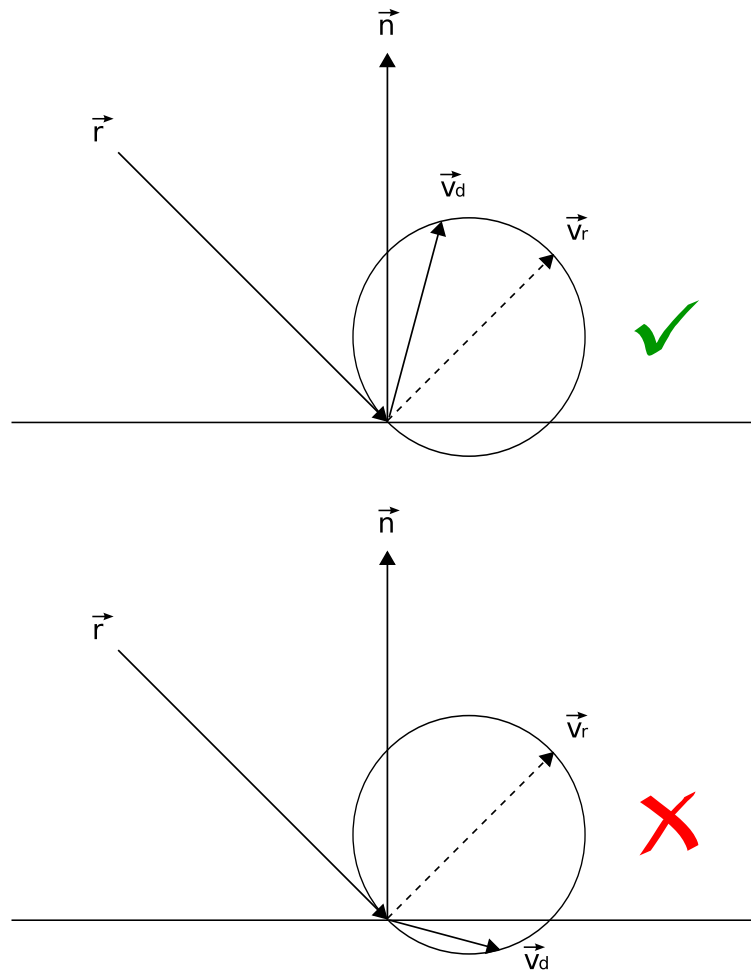


Figure 3.2: Rejection sampling for reflected ray. Top: $\vec{v}_d \cdot \vec{n} > 0$, ray accepted. Bottom: $\vec{v}_d \cdot \vec{n} < 0$, ray rejected (requires new sample).

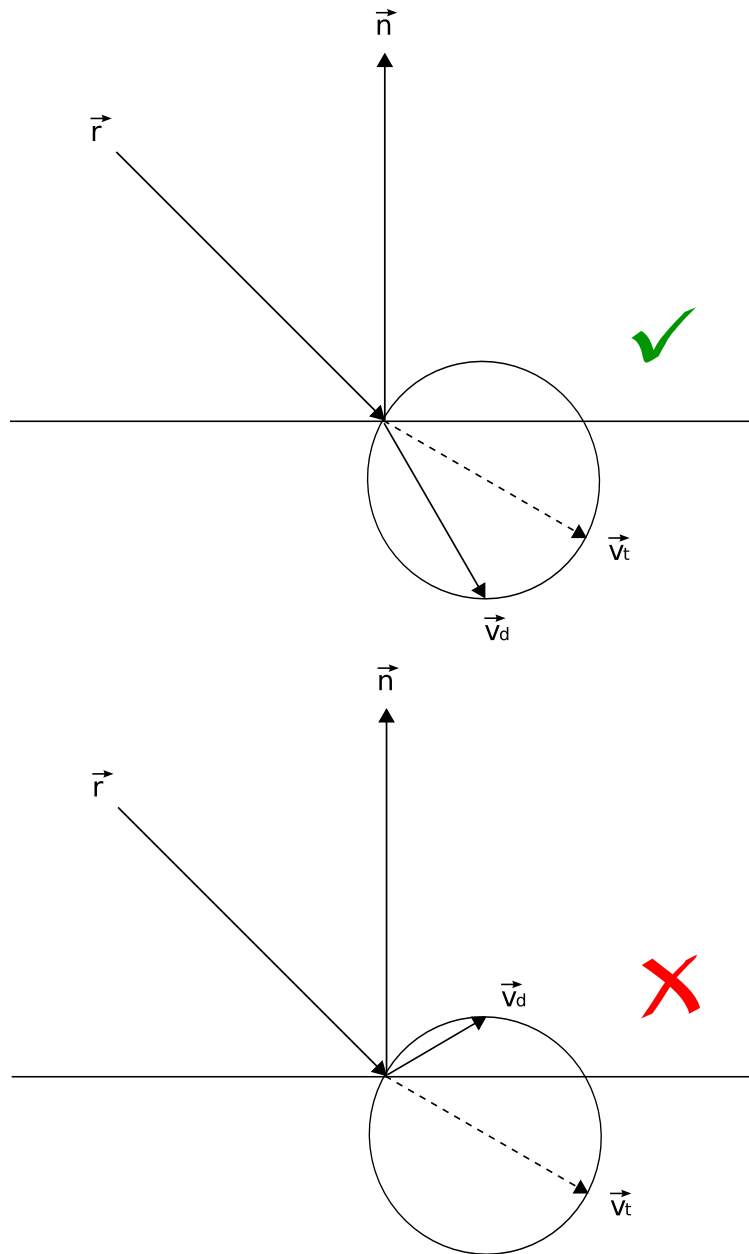


Figure 3.3: Rejection sampling for transmitted ray. Top: $\vec{v}_d \cdot \vec{n} < 0$, ray accepted. Bottom: $\vec{v}_d \cdot \vec{n} > 0$, ray rejected (requires new sample).

3.3 Absorption

When a ray is traversing either the ABL or the Stromal Layer, the ILIT model tests for its possible absorption (Figure 3.4) due to the presence of pigments (Section 2.2). As described by Prahl [66], the probability of absorption of a photon (ray) traveling a distance Δp at a certain wavelength λ in a medium is given by :

$$P_{\mu_a}(\lambda) = 1 - \exp(-\mu_a(\lambda)\Delta p), \quad (3.2)$$

where $\mu_a(\lambda)$ represents the absorption coefficient of the medium for wavelength λ . The absorption coefficient is obtained by adding the absorption coefficients of the medium's constituent materials, which, in turn, are computed by multiplying their spectral molar absorption (extinction) coefficient by their concentration in the medium.

In the case of the ABL, this probability is obtained using:

$$P_{\mu_{a_A}}(\lambda) = 1 - \exp\left(-\mu_{a_A}(\lambda)\frac{h_A}{\cos \theta}\right), \quad (3.3)$$

where $\mu_{a_A}(\lambda)$ represents the absorption coefficient of the ABL, which is computed using the concentrations of eumelanin and pheomelanin present in this tissue (Section 2.2), h_A represents to the thickness of the ABL, and $|\theta| < 90^\circ$ corresponds to the angle between the ray direction and the tissue's normal direction.

If $P_{\mu_{a_A}}(\lambda) \leq u_4$, then the ray is absorbed. Otherwise, the ray is propagated until it reaches the next interface.

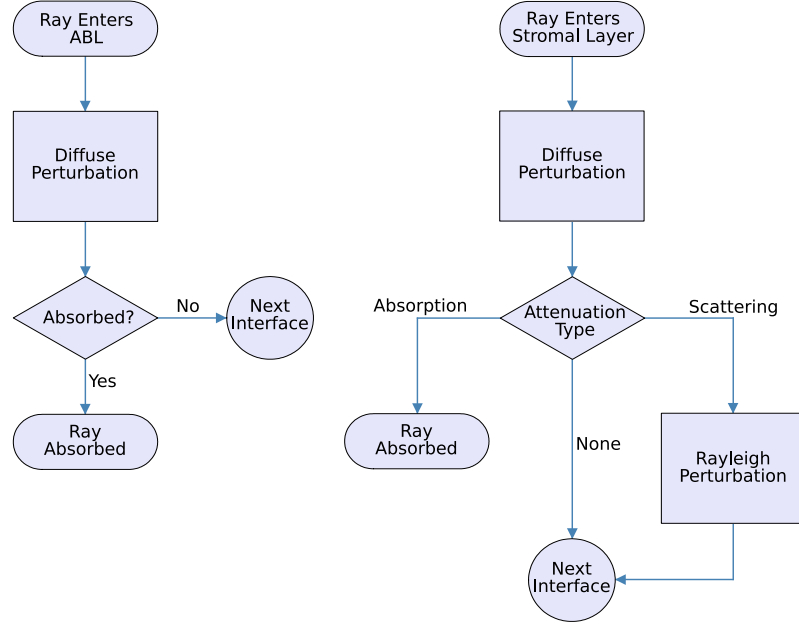


Figure 3.4: Flowcharts illustrating the algorithms used by the ILIT model to simulate light transport in the ABL (left) and Stromal Layer (right).

In the Stromal Layer, the test for absorption is combined with the test for Rayleigh scattering, and these are described in more detail in the following section.

3.4 Attenuation and Scattering

When a ray traverses the Stromal Layer, it may be attenuated (Figure 3.4). An attenuation event can be represented by either an absorption or a scattering event, and the attenuation coefficient, $\mu(\lambda)$, is simply the sum of the absorption and scattering coefficients.

The former, in this case, corresponds to the absorption coefficient of the Stromal Layer, $\mu_{aS}(\lambda)$, which is computed using the concentrations of melanins, hemoglobins

and carotenoids present in this tissue (Section 2.2). The latter is derived in this section in terms of Rayleigh scattering caused by stromal collagen fibrils (Section 2.2).

It is assumed that the volume occupied by each collagen fibril of radius r can be approximated by a small sphere with the same radius [45], which results in a scatterer density given by:

$$N = \left(\frac{4}{3} r^3 \pi \right)^{-1} f_{col}, \quad (3.4)$$

where f_{col} corresponds to the volume fraction of the tissue occupied by the scatterers (the collagen fibrils). Using this density, the scattering coefficient can be computed using the following expression [55, 80]:

$$\mu_s(\lambda) = \frac{8\pi^3}{3N} ((\eta(\lambda))^2 - 1)^2 (\lambda^{-4}), \quad (3.5)$$

where η represents the refractive index of the scatterers.

Equation 3.5 was originally developed for the study of atmospheric scattering [55, 80]. However, unlike atmospheric simulations where the scatterers are usually assumed to be dispersed in vacuum, our simulations need to account for the fact that the collagen fibrils, with their own refractive index η_{col} , are dispersed in iridal base material with a refractive index $\eta_{base} \neq 1.0$. Hence, in our simulations, η in Equation 3.5 is replaced by the ratio $\eta_{col}(\lambda)/\eta_{base}(\lambda)$.

After computing the absorption and scattering coefficients, the attenuation

probability is obtained using:

$$P_\mu(\lambda) = 1 - \exp\left(-\mu(\lambda) \frac{h_S}{\cos \theta}\right), \quad (3.6)$$

where h_S represents the thickness of the Stromal Layer, and $|\theta| < 90^\circ$ corresponds to the angle between the ray direction and the tissue's normal direction.

If $u_5 > P_\mu(\lambda)$, then neither absorption nor scattering occurs. Otherwise, we need to determine the attenuation type. For this purpose, the absorption probability is computed as follows:

$$P_{\mu_{a_S}}(\lambda) = \frac{\mu_{a_S}(\lambda)}{\mu(\lambda)}. \quad (3.7)$$

If $u_6 \leq P_{\mu_{a_S}}(\lambda)$, then the ray is absorbed. Otherwise, the ray is scattered, and its new direction is determined according to the Rayleigh scattering phase function [87], *i.e.*, using rejection sampling, we repeatedly generate the polar perturbation angle:

$$\alpha_R = 2\pi u_7,$$

and accept it only when

$$u_8 \leq 0.5(1 + \cos^2 \alpha_R).$$

Since the directional perturbation in the azimuthal direction is symmetric [87], the azimuthal perturbation angle is simply given by $\beta_R = 2\pi u_9$. Hence, the new ray direction is obtained by perturbing it according to the angular displacements given by α_R and β_R ¹.

¹To eliminate numerical instability introduced by indefinite total internal reflections, in the ILIT model, a ray is treated as absorbed after 400 interface transitions without being absorbed nor released from the iris. In our experiments, these rays account for an insignificant amount of samples (a maximum of 80 rays observed out of 780 million rays that covers the iris area).

Chapter 4

Evaluation Issues

In this chapter, we describe the procedures and the biophysical data set used in the evaluation of the ILIT model.

4.1 Procedures

In order to assess the accuracy and predictability of the proposed model, we compared modeled results with actual iridal data measured by Imai [41] and Unander [86], as well as qualitative reports on the iridal spectral and spatial light distributions available in the scientific literature. For the latter, virtual measurement devices [3, 49] were implemented to allow the gathering of modeled reflectance and BRDF (bidirectional reflectance distribution function) data. For the former, the computational experiments took into account the actual measurement conditions to avoid the introduction of bias in the comparisons. For example, to obtain model

readings in terms of the radiometric quantity measured by Imai [41] and Unander [86], namely reflected radiance, the number of rays per wavelength shot towards the virtual iridal specimen was modulated (Appendix A) according to the spectral characteristics of the light source used in the actual measurements. In addition, since the actual measurements were performed under *in vivo* conditions, the refractive indices of the tear layer, cornea and the aqueous humor, represented by $\eta_{tear}(\lambda)$, $\eta_{cor}(\lambda)$ and $\eta_{ah}(\lambda)$ respectively, were used to determine the fraction of light incident on the virtual iridal specimen. We note, however, that no compensation was applied to account for a possible wavelength dependency of the cornea and aqueous humor transmittances [8]. This decision was made based on the observation that, to the best of our knowledge, the compensation formulas currently available in the literature [8, 4, 88] were obtained by applying fitting approaches to data whose measurement did not account for backscattering [8, 4, 88]. Another simulation decision taken to match the actual experiment set up was the elimination of the rays directly reflected from the tear layer. We note that specular reflections were carefully excluded by Imai [41] and Unander [86] in the actual measurements.

4.2 Data

The quantitative values used for the model parameters were chosen according to data published in the biophysical literature. For certain parameters, however, data is not readily available, and it was necessary to derive approximated values from existing data. For example, to obtain the refractive indices for the ABL and the Stromal Layer, we applied the Gladstone and Dale’s law [56, 84], which states

that the refractive index of a given material can be expressed by the sum of the refractive indices of its components, each weighted by the volume fraction occupied by the respective component. Accordingly, the following expression was used for the refractive index of the ABL:

$$\eta_A(\lambda) = \eta_{fib}(\lambda) f_{fib} + \eta_{base}(\lambda) (1 - f_{fib}), \quad (4.1)$$

where $\eta_{fib}(\lambda)$ and f_{fib} represent the refractive index and the volume fraction of the fibroblasts respectively. Similarly, the following expression was used for the refractive index of the Stromal Layer:

$$\eta_S(\lambda) = \eta_{col}(\lambda) f_{col} + \eta_{base}(\lambda) (1 - f_{col}). \quad (4.2)$$

For the IPE, based on its morphological characteristics (Section 2.2), a suitable approximation corresponds to the refractive index of the ocular base material [47]. This approximation was used in our simulations. Although refractive indices are wavelength dependent quantities, we remark that, for ocular materials, usually a single value over the visible range is available in the literature. The refractive indices used in the evaluation of the ILIT model are given in Table 4.1, and the values for f_{fib} and f_{col} correspond to $1/3$ and $\pi/(4 \sin(\pi/3))$ respectively. The former was provided by Snell and Lemp [77], and the later was obtained by considering stromal collagen fibrils with radius equal to $30nm$ [77] distributed in an hexagonal arrangement with a periodicity of $60nm$ [77].

Also due to the fact that the actual measurements were performed under *in vivo*

Table 4.1: Refractive indices used in the simulations.

Symbol	Value	Source
η_{air}	1.0003	[74]
η_{tear}	1.337	[22]
η_{cor}	1.3771	[102]
η_{ah}	1.336	[24]
η_{fib}	1.42	[47]
η_{base}	1.5	[47]
η_{col}	1.47	[84, 85]

conditions, we cannot determine the exact values for the thickness of the subjects' iridal layers. Hence, we used $h_A = 0.05675mm$ and $h_S = 0.2855mm$ in our simulations, which correspond to average values provided in the biomedical literature [64, 23]. For the same reason, the values for the pigment concentrations, which are provided below, were chosen according to average ranges reported for different pigmentation levels in the biomedical literature [7, 25, 69], and considering a virtual iridal specimen with a diameter of $11mm$ [64, 96], which accounts for a pupil radius of $2.5mm$ [64]. For detailed derivation, see Appendix B.

The spectral properties of three different types of irides were considered in the actual measurements, namely lightly, moderately and heavily pigmented. The melanin concentration values used in the evaluation of the ILIT model are given in Table 4.2, and they were computed from data measured by Prota *et al.* [69] for different iridal types.

The concentrations for the oxyhemoglobin and deoxyhemoglobin, $0.042mmol/l$ and $0.042mmol/l$ respectively, were obtained by assuming that the Stromal Layer contains approximately 4% of blood [45], and taking into account that the concentration of hemoglobin in blood is typically $2.1mmol/l$ [25]. The values se-

lected for the lutein and zeaxanthin concentrations were $1.562 \times 10^{-4} mg/ml$ and $5.968 \times 10^{-5} mg/ml$ respectively, and they were computed from data provided by Bernstein *et al.* [7].

Table 4.2: Melanin concentrations (mg/ml) used in the simulations.

Pigment	Pigmentation Level		
	High	Moderate	Low
eumelanin	1.008	0.8138	0.1201
pheomelanin	0.2674	0.2054	0.0194

In our experiments, we used spectral molar absorptions curves for melanins and hemoglobins available at the Oregon Medical Laser Center [65, 44], and spectral molar absorptions curves for carotenoids provided by Zscheile *et al.* [103] (Figure 2.2).

We also account for the lengthening of the optical path of a tissue due to the inhomogeneous distribution of pigments under *in vivo* conditions [20, 28]. This lengthening is called factor of intensification¹ since it may result in an absorption increase when a pigment’s concentration exceeds a certain threshold [72, 90]. Based on values reported in the tissue optics literature for natural pigments with similar concentrations [72, 90], we apply a factor of intensification of 2.2 to the melanin absorption curves used in our experiments (Appendix D).

¹In near-infrared spectroscopy applications, this lengthening is usually referred to as the differential path length factor [20, 54].

Chapter 5

Results and Discussion

5.1 Quantitative Predictions

Quantitative comparisons of model readings with actual data measured by Imai [41] and Unander [86] for three iridal specimens (lightly pigmented, moderately pigmented and heavily pigmented) are presented in Figure 5.1. These comparisons indicate a good quantitative and qualitative agreement between modeled and measured curves. The results provided by the ILIT model were obtained using the data provided in the previous section, and considering an equal distribution of melanin between the ABL and the Stromal Layer.

As mentioned in Section 2.2, biophysical parameters such as pigment concentration and tissue thickness are not uniform across the human iris. Hence, the measured spectral responses may vary depending on the measurement position. The variations observed in the experiments by Imai [41] and Unander [86] are

represented by error bars in the graphs presented in Figure 5.1. For the heavily pigmented specimen, the modeled curve is slightly outside the measured range. For the moderately and lightly pigmented specimens, the modeled curves are almost entirely within the variation range observed in the actual measurements.

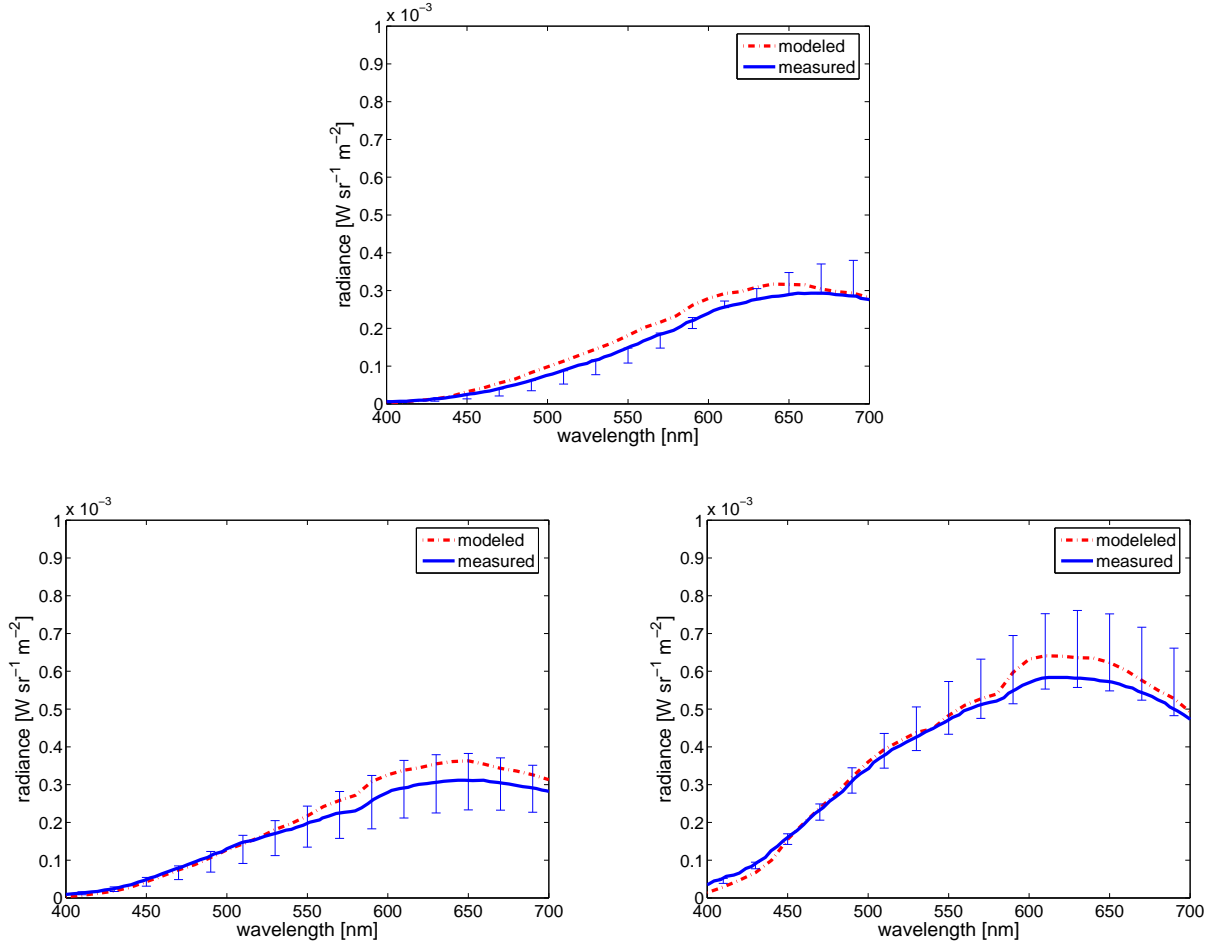


Figure 5.1: Comparison of modeled reflected radiance curves provided by the ILIT model with actual reflected radiance curves measured by Imai [2000] and Unander [2000]. Top: heavily pigmented iris specimen. Bottom left: moderately pigmented specimen. Bottom right: lightly pigmented specimen. The error bars indicate maximum and minimum values observed in the actual measurements.

Two aspects shall be taken into account in the analysis of these quantitative

comparisons. First, we remark that the model input (characterization) data correspond to the best possible match that we could obtain between the specimens’ description and data available in the literature, which, in several instances, correspond to average values. Hence, although the ILIT model can qualitatively simulate different spectral responses due to the variation of parameters such as pigment concentration and tissue thickness (Section 5.2), the quantitative accuracy of its predictions is limited by the availability of precise iridal characterization data, and the modeled curves presented in this paper can be viewed as average results themselves. Second, recall that biological data are usually obtained under *in vitro* conditions, and one may expect deviations from *in vivo* values [20]. For example, the measurement of the extinction coefficient of a given pigment usually involves its dissolution using an organic solvent, and small spectral shifts caused by changes in the molecular properties of the pigments can be observed [28, 11, 12].

5.2 Qualitative Predictions

Besides the quantitative comparisons described above, we also performed qualitative comparisons against actual observations of real phenomena to assess the predictability of the ILIT model. As verified by Delori *et al.* [16], the reflectance spectra of lightly pigmented irides present a characteristic blood signature (“w” shape) between $500nm$ to $600nm$ due to the characteristics of the absorption spectra of hemoglobin (Figure 2.2) [44], and this signature is not detectable in irides whose absorption spectra is dominated by melanins. The modeled reflectance curves presented in Figure 5.2 show that the ILIT model can account for this phenomenon. It

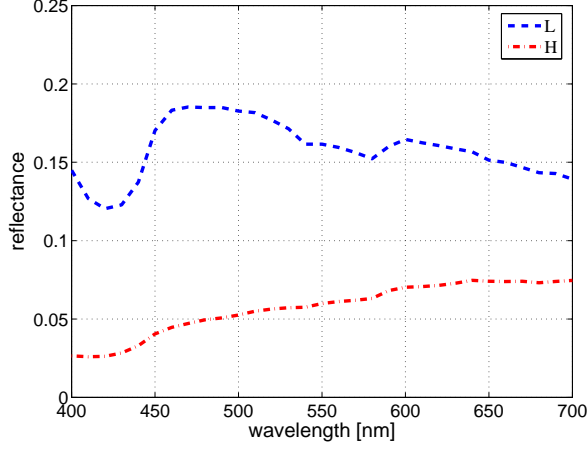


Figure 5.2: Comparison of modeled reflectance curves provided by the ILIT model considering specimens with different levels of pigmentation: low (L) and high (H).

can also be observed in the modeled reflected radiance curves (Figure 5.1) as the dip between $550nm$ to $600nm$ increases when the melanin concentration is reduced. Delori *et al.* [16] also observed that iris reflectance among subjects with different levels of pigmentation varies most significantly at short wavelengths, reaching its maximum around $450nm$. In addition, the range of this reflectance variation starts to decrease continuously around $600nm$. These characteristics of iridal reflectance spectra can also be observed in the modeled reflectance curves presented in Figure 5.2. Incidentally, the premise that the iris becomes lighter (higher reflectance) as the melanin concentration decreases [97, 100] can also be verified in the modeled results shown in Figure 5.2.

According to observations by Menon *et al.* [59] and Imesh *et al.* [42], the distribution of the iridal melanin can also be a determinant of iridal chromatic attributes, with a more pigmented ABL resulting in a darker (lower reflectance) iris. We performed simulations to assess the predictability of the ILIT model with respect to

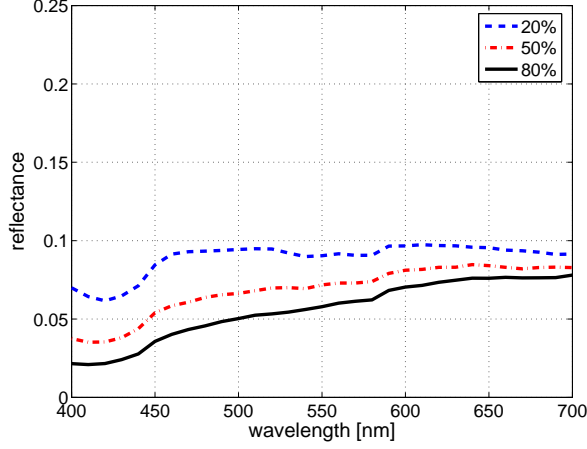


Figure 5.3: Comparison of modeled reflectance curves provided by the ILIT model considering different melanin distributions between the ABL and the Stromal Layer (expressed in terms of the percentage of melanin presented in the ABL).

this phenomenon. For these simulations we selected, without loss of generality, a moderately-pigmented iris specimen, and we varied the distribution of melanin between the ABL and the Stromal Layer. The results shown in Figure 5.3 indicate that the ILIT model can qualitatively account for these chromatic variations.

Our qualitative experiments also included the verification of the iridal spatial light distributions provided by the ILIT model (expressed in terms of BRDFs). Although its role on the visual appearance of the human eye may be not as significant as the iridal spectral signature, its characteristics can provide additional evidence of the correctness of the simulation algorithms used by the ILIT model. Figure 5.4 presents plots of modeled BRDFs obtained for iridal specimens with different levels of pigmentation. As illustrated in these plots, the modeled BRDFs exhibit a near-Lambertian distribution which, as mentioned earlier (Section 2.2), corresponds to the general scattering profile of real human irides [10, 91, 96].

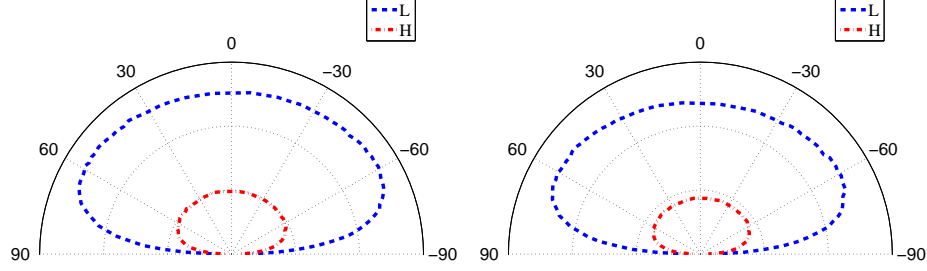


Figure 5.4: Modeled iridal BRDFs measured at $550nm$. Left: considering an angle of incidence of 0° . Right: considering an angle of incidence of 60° . Plots correspond to scattering profiles taken at the principal plane of incidence, and considering specimens with different levels of pigmentation, namely low (L) and high (H).

Finally, in order to further illustrate the predictability of the ILIT model, we generated images using a standard rendering framework, whose main algorithm and parameters are described in Appendix C. Figure 5.5 presents images rendered using the ILIT model (iris pattern and sclera taken from a photo), and taking as input the data provided in the previous section. These images illustrate chromatic variations obtained by changing the concentration and distribution of iridal melanins. We remark that the iridal chromatic attributes depicted in these images correspond solely to spectral signatures provided by the ILIT model, *i.e.*, to avoid the introduction of bias in our observations, post-processing tone adjustment techniques [32] were not applied.

As mentioned earlier, the thickness of the tissues is not uniform across the human iris, and there are regions characterized by higher pigment concentration. For example, Figure 5.6 illustrates spectral changes resulting from reducing the thickness of the iridal tissues of specimens characterized by eumelanin concentration of $0.1201mg/ml$ and pheomelanin concentration of $0.0194mg/ml$. As expected, a



Figure 5.5: Images showing iridal chromatic variations obtained using the ILIT model. From left to right, the iridal eumelanin concentration was decreased from $1.008mg/ml$ to $0.1201mg/ml$, and the iridal pheomelanin concentration from $0.2674mg/ml$ to $0.0194mg/ml$. From top to bottom, the percentage of melanin presented in the ABL was altered: 20% (top row), 50% (middle row) and 80% (bottom row).

thickness reduction is followed by an increase in pigmentation concentration and a hue transition from blue to a slightly darker blue with a hint of grey.

Finally, Figure 5.7 shows spectral changes when the pheomelanin concentration is increased in an iris with a fixed eumelanin concentration of $0.1201mg/ml$, since Prota *et al.* [69] reported a positive correlation between green irides and pheomelanin. Although the renders do not clearly demonstrate this correlation, it could be due to the choice of colour space (See Appendix C).

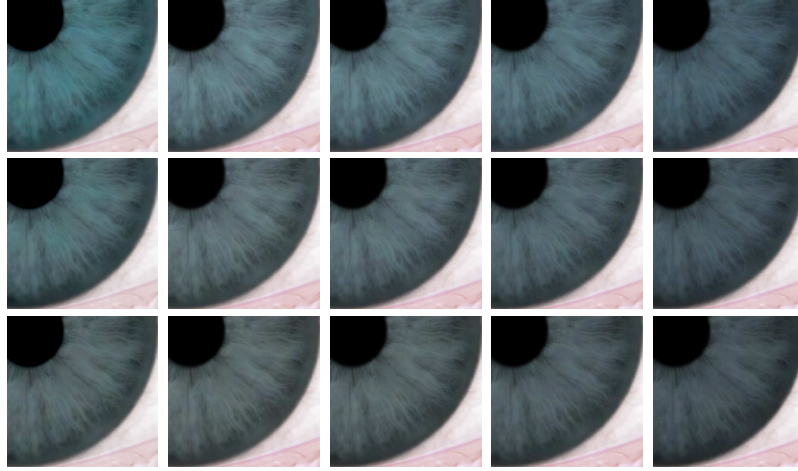


Figure 5.6: Images showing iridal chromatic variations of a lightly pigmented iris (eumelanin concentration: $0.1201mg/ml$, pheomelanin concentration: $0.0194mg/ml$) obtained by varying the thickness of the ABL and the Stromal Layer. From left to right: Iris thickness is decreased by 0%, 5%, 15%, 30% and 50%. From top to bottom, the percentage of melanin presented in the ABL was altered: 20% (top row), 50% (middle row) and 80% (bottom row).

5.3 Rendering Performance

A non-optimized implementation of the rendering framework described in Appendix C running on a 2 GHz AMD Athlon CPU takes about 20 hours to render an iris model with 6 billion samples, which calculates to be around 80000 samples per second.

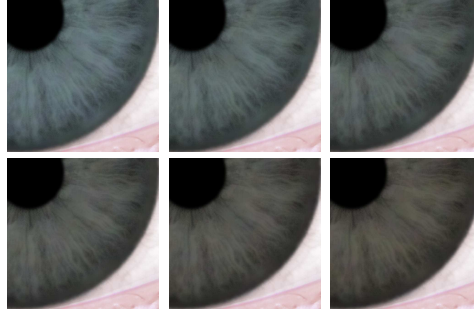


Figure 5.7: Images showing iridal chromatic variations of a lightly pigmented iris (eumelanin concentration: 0.1201mg/ml) obtained by increasing the pheomelanin concentration. (From left to right) Top: pheomelanin concentrations of 0.0388mg/ml , 0.1164mg/ml , 0.194mg/ml . Bottom: 0.2716mg/ml , 0.3492mg/ml , 0.4268mg/ml

Chapter 6

Conclusion and Future Work

The ILIT model is the first biophysically-based computer model proposed to simulate both the scattering and spectral properties of the human iris. However, it shall be considered as a step in the right direction instead of a final modeling solution for the light interactions with iridal tissues. Its evaluation showed a general quantitative agreement between modeled results and actual measured data. It also indicated that there is still room for further research in this area, which will likely depend on the acquisition of more comprehensive iridal data sets including both specimen's characterization data and spectral measurements.

Since quantitative evaluations may be affected by inherent difficulties to characterize testing specimens, we believed that qualitative evaluations are also required to assess the predictability of a computer model. In the case of the ILIT model, the qualitative agreement between modeled results and observations of actual phenomena reported in the scientific literature represents additional evidence of its

predictive capabilities.

The algorithmic formulation of the ILIT model is based on standard Monte Carlo techniques which are sufficiently flexible to allow the modeling of complex phenomena within the iridal tissues. The stochastic simulations performed by the model, however, may be time consuming and represent a bottleneck in an image synthesis pipeline. Alternatively, these simulations could be either run off-line, and the quantities computed by the model stored and reconstructed on the fly during rendering, or performed using dedicated graphics hardware. We plan to investigate these implementation alternatives in the next stage of our research.

As future work, we also intend to exploit the ILIT model on the assessment of theories and data relating iridal chromatic attributes to ocular medical conditions, and to extend our investigations to other ocular tissues and media. Although a reasonable amount of research on these materials is available in the biomedical literature, the computer graphics simulation of phenomena such as corneal polarization and tear film interference will require wave optics modeling tools to be brought to bear on the problem.

Bibliography

- [1] *Colorimetry official recommendations of the international commission on illumination*, Tech. report, Commission Internationale de L'Eclairage (CIE), Paris, France, 1970.
- [2] D.M. Albert, W.R. Green, M.L. Zimbric, C. Lo, R.E. Gangnon, K.L. Hope, and J. Gleiser, *Iris melanocytes numbers in Asian, African American, and Caucasian irides*, Transactions of the American Ophthalmological Society **101** (2003), 217–222.
- [3] G.V.G. Baranoski, J.G. Rokne, and G. Xu, *Virtual spectrophotometric measurements for biologically and physically based rendering*, The Visual Computer **17** (2001), 506–508.
- [4] E.M. Beems and J. van Best, *Light transmission of the cornea in the whole human eyes*, Experimental Eye Research **50** (1990), 393–395.
- [5] I. Bell and G.V.G. Baranoski, *More than rgb: Moving toward spectral color reproduction*, ACM SIGGRAPH 2003 course 24, San Diego, CA, July 2003 (2003).

- [6] O. Bergamin, A. Schoetzau A, K. Sugimoto, and M. Zulauf, *The influence of iris color on the pupillary light reflex*, Graefes Arch. Clin. Exp. Ophthalmol. **236** (1998), no. 8, 567–570.
- [7] P.S. Bernstein, F. Khachik, L.S. Carvalho, G.J. Muir, D. Zhao, and N.B. Katz, *Identification and quantitation of carotenoids and their metabolites in the tissues of the human eye*, Experimental Eye Research **72** (2001), 215–223.
- [8] E.A. Boettner and J.R. Wolter, *Transmission of the ocular media*, Investigative Ophthalmology and Visual Science **1** (1962), no. 6, 776–783.
- [9] R.M. Bolle, S. Pankanti, J.H. Connel, and N.K. Ratha, *Iris individuality: A partial iris model*, 17th International Conference on Pattern Recognition -ICPR'04, 2004, pp. 927–930.
- [10] J.M. Bueno and F. Vargas-Martin, *Measurements of the corneal birefringence with a liquid-crystal imaging polariscope*, Applied Optics **41** (2002), no. 1, 116–124.
- [11] C. Buschmann and E. Nagel, *Reflection spectra of terrestrial vegetation as influenced by pigment-protein complexes and the internal optics of the leaf tissue*, IGARSS'91 15th International Geoscience and Remote Sensing Symposium (Espoo, Finland), vol. 4, 1991, pp. 1909–1912.
- [12] E.W. Chappelle, M.S. Kim, and J.E. McMurtrey, *Ratio analysis of reflectance spectra (RARS): An algorithm for the remote estimation of the concentrations of chlorophyll A, chlorophyll b, and carotenoids in soybean leaves*, Remote Sensing of Environment **39** (1992), 239–247.

- [13] CIE, *International congress on illumination*, International Congress on Illumination 1931 (Cambridge, England), Cambridge University Press, 1931.
- [14] J. Daugman and C. Dowing, *Epigenetic randomness, complexity and singularity of human iris patterns*, Proc. R. Soc. Lond. B **268** (2001), 1737–1740.
- [15] M.F. Deering, *A photon accurate model of the eye*, ACM Transactions on Graphics **24** (2005), no. 3, 649–658.
- [16] F.C. Delori, C.K. Dorey, and K.A.Fitch, *Characterization of ocular melanin by iris reflectometry*, Investigative Ophthalmology and Visual Science **32** (1991), no. 1-4, 1144.
- [17] F.C. Delori, C.K. Dorey, G. Staurenghi, O. Arend, D.G. Goger, and J.J. Weiter, *In vivo fluorescence of the ocular fundus exhibits retinal pigment epithelium lipofuscin characteristics*, Investigative Ophthalmology and Visual Science **36** (1995), no. 3, 718–729.
- [18] F.C. Delori, D.G. Goger, and C.K. Dorey, *Age-related accumulation and spatial distribution of lipofuscin in rpe of normal subjects*, Investigative Ophthalmology and Visual Science **42** (2001), no. 8, 1855–1866.
- [19] F.C. Delori and K.P. Pflibsen, *Spectral reflectance of the human ocular fundus*, Applied Optics **28** (1989), no. 6, 1061–1077.
- [20] D.T. Delpy, M. Cope, P. Zee, S. Arridge, S. Wray, and J. Wyatt, *Estimation of optical pathlength through tissue from direct time of flight measurement*, Physics in Medicine and Biology **33** (1988), no. 12, 1433–1442.

- [21] C. Donner and H.W. Jensen, *Light diffusion in multi-layered translucent materials*, ACM Transactions on Graphics **24** (2005), no. 3, 1032–1039.
- [22] F. Duck, *Physical properties of tissue: A comprehensive reference book*, Academic Press Inc., California, U.S.A., 1990.
- [23] R.C. Eagle, *Iris pigmentation and pigmented lesions: An ultrastructural study*, Trans. Am. Ophth. Soc. **86** (1988), 581–687.
- [24] H.F. Edelhauser, D.L.V. Horn, and R.E. Records, *Cornea and sclera*, Physiology of the Human Eye and Visual System (Maryland, U.S.A.) (R.E. Records, ed.), Harper and Row Publishers Inc., 1979, pp. 68–97.
- [25] R. Flewelling, *Noninvasive optical monitoring*, The Biomedical Engineering Handbook (Boca Raton, FL, USA) (J.D. Bronzino, ed.), IEEE Press, 2000, Section 86, pp. 1–11.
- [26] J.V. Forrester, A.D. Dick, P.G. McMenemy, and W.R. Lee, *The eye: Basic sciences in practice*, second ed., WB Saunders, Sydney, 2002.
- [27] D.E. Freund, R.L. McCally, and R.A. Farrell, *Effects of fibril orientations on light scattering in the cornea*, J. Opt. Soc. Am. **3** (1986), no. 11, 1970–1982.
- [28] L. Fukshansky, *Absorption statistics in turbid media*, Journal of Quantitative Spectroscopy and Radiative Transfer **38** (1987), no. 5, 389–406.
- [29] L. Geng, U. Wihlmark, and P.V. Algvere, *Lipofuscin accumulation in iris pigment epithelial cells exposed to photoreceptor outer segments*, Experimental Eye Research **69** (1999), 539–546.

- [30] E.J. German, M.A. Hurst, D. Wood, and J. Gilchrist, *A novel system for the objective classification of iris colour and its correlation with response to 1% tropicamide*, Ophthal. Physiol. Opt. **18** (1998), no. 2, 103–110.
- [31] A.S. Glassner, *Principles of digital image synthesis*, Morgan Kaufmann Publishers, San Francisco, C.A., U.S.A., 1995.
- [32] D.P. Greenberg, J. Arvo, E. Lafortune, K.E. Torrance, J.A. Ferwerda, B. Walter, B. Trumbore, P. Shirley, S. Pattanaik, and S. Foo, *A framework for realistic image synthesis*, SIGGRAPH, Annual Conference Series, 1997, pp. 477–494.
- [33] R. Hall, *Comparing spectral color computation methods*, IEEE Computer Graphics and Applications **19** (1999), no. 4, 36–45.
- [34] M.A. Halstead, B.A. Barsky, S.A. Klein, and R.B. Mandell, *Reconstructing curved surfaces from specular reflection patterns using spline surface fitting of normals*, SIGGRAPH, Annual Conference Series, 1996, pp. 335–342.
- [35] M. Hammer, A. Roggant, D. Schweitzer, and G. Muller, *Optical properties of ocular fundus tissues - and in vitro study using the double-integrating-sphere technique and inverse Monte Carlo simulation*, Physics in Medicine and Biology **40** (1995), 963–978.
- [36] M. Hammer and D. Schweitzer, *Quantitative reflection spectroscopy at the human ocular fundus*, Physics in Medicine and Biology **47** (2002), 179–191.

- [37] J.M. Hammerley and D.C. Handscomb, *Monte carlo methods*, Wiley, New York, 1964.
- [38] P. Hanrahan and W. Krueger, *Reflection from layered surfaces due to sub-surface scattering*, SIGGRAPH, Annual Conference Series, August 1993, pp. 165–174.
- [39] F.G. Holz, B. Piguet, D.C. Minassian A.C. Bird, and R.A. Weale, *Decreasing stromal iris pigmentation as a risk factor for age-related macular degeneration*, Am. J. Ophthalmol. **117** (1994), 19–23.
- [40] R.S. Hunter and R.W. Harold, *The measurement of appearance*, second ed., John Wiley & Sons, New York, 1987.
- [41] F.H. Imai, *Preliminary experiment for spectral reflectance estimation of human iris using a digital camera*, Tech. report, Munsell Color Science Laboratory, Rochester Institute of Technology, Rochester, N.Y., U.S.A., 2000.
- [42] P.D. Imesch, C.D. Bindley, Z. Khademian, B. Ladd, R. Gangnon, D.M. Albert, and I.H.L. Wallow, *Melanocytes and iris color, electron microscopic findings*, Archives of Ophthalmology **114** (1996), 443–447.
- [43] P.D. Imesch, I.H.L. Wallow, and D.M. Albert, *The color of the human eye: A review of morphologic correlates and of some conditions that affect iridial pigmentation*, Survey of Ophthalmology **41** (1997), no. suppliment 2, S117–S123.

- [44] S. Jacques, *Optical absorption of melanin*, Tech. report, Oregon Medical Laser Center, Portland, U.S.A, 2001.
- [45] S.L. Jacques, *Origins of tissue optical properties in the uva visible and nir regions*, OSA TOPS on Advances in Optical Imaging and Photon Migration **2** (1996), 364–369.
- [46] J.T. Kajiya, *The rendering equation*, ACM SIGGRAPH 1986 (August 1986), vol. 20, 1986, pp. 143–150.
- [47] N.G. Khlebtsov, I.L. Maksimova, V.V. Tuchin, and L.V. Wang, *Introduction to light scattering by biological objects*, Handbook of Optical Biomedical Diagnostics (Bellingham, U.S.A.) (V.V. Tuchin, ed.), SPIE Press, 2002, pp. 31–167.
- [48] A. Krishnaswamy and G.V.G. Baranoski, *A biophysically-based spectral model of light interaction with human skin*, Computer Graphics Forum **23** (2004), no. 3, 331–340.
- [49] A. Krishnaswamy, G.V.G. Baranoski, and J.G. Rokne, *Improving the reliability/cost ratio of goniophotometric measurements*, Journal of Graphics Tools **9** (2004), no. 3, 31–51.
- [50] A. Lefohn, R. Caruso, E. Reinhard, B. Budge, and P. Shirley, *An ocularist’s approach to human iris synthesis*, IEEE Computer Graphics and Applications **23** (2003), no. 6, 70–75.
- [51] S. Lerman, *Radiant energy and the eye*, Macmillan, Hampshire, U.K., 1980.

- [52] C. Lilley, F. Lin, W.T. Hewitt, and T.L.J. Howard, *Colour in computer graphics*, Tech. report, ITTI Computer graphics and Visualisation, Manchester Computing Centre, University of Manchester, UK, December 1993, 1993.
- [53] S.R. Marschner, H.W. Jensen, M. Cammarano, S. Worley, and P. Hanrahan, *Light scattering from human hair fibers*, ACM Transactions on Graphics **22** (2003), no. 3, 780–791.
- [54] S.J. Matcher, M. Cope, and D.T. Delpy, *Use of the water absorption spectrum to quantify tissue chromophore concentration changes in near-infrared spectroscopy*, Physics in Medicine and Biology **38** (1993), 177–196.
- [55] E.J. McCartney, *Optics of the atmosphere: Scattering by molecules and particles*, John Wiley & Sons Inc., 1976.
- [56] K.M. Meek, S. Dennis, and S. Khan, *Changes in the refractive index of the stroma and its extrabibrillar matrix when the cornea swells*, Biophysical Journal **85** (2003), 2205–2212.
- [57] M. Melgosa, M.J. Rivas, L. Gómez, and E. Hita, *Towards a colorimetric characterization of the human iris*, Ophthal. Physiol. Opt. **20** (2000), no. 3, 252–260.
- [58] I.A. Menon, P.K. Basu, S. Persad, M. Avaria, C.C. Felix, and B. Kalyanaraman, *Is there any difference in the photobiological properties of melanins isolated from human blue and brown eyes?*, British Journal of Ophthalmology **71** (1987), 549–552.

- [59] I.A. Menon, D.C. Wakeham, S.D. Persad, M. Avaria, Graham E. Trope, and P.K. Basu, *Quantitative determination of the melanin contents in ocular tissues from human blue and brown eyes*, Journal of Ocular Pharmacology **8** (1992), no. 1, 35–42.
- [60] R.A. Moses, *Adler's physiology of the eye, clinical applications*, St. Louis: The C. V. Mosby Company, Missouri, U.S.A., 1970.
- [61] R. Narayanswamy, G.E. Johnson, P.E.X. Silveira, and H.B. Wach, *Extending the imaging volume for biometric iris recognition*, Applied Optics **44** (2005), no. 5, 701–712.
- [62] C.S. Ng and L. Li, *A multi-layered reflection model of natural human skin*, Computer Graphics International 2001 (Hong Kong), July 2001, pp. 249–256.
- [63] F.E. Nicodemus, J.C. Richmond, J.J. Hsia, I.W. Ginsberg, and T. Limperis, *Geometrical considerations and nomenclature for reflectance*, Physics-Based Vision Principles and Practice: Radiometry (Boston) (L.B. Wolff, S.A. Shafer, and G.E. Healey, eds.), Jones and Bartlett Publishers, 1992, pp. 94–145.
- [64] J. Nolte, *Iris and pupil*, Physiology of the Human Eye and Visual System (Maryland, U.S.A.) (R.E. Records, ed.), Harper and Row Publishers Inc., 1979, pp. 217–231.
- [65] S. Prahl, *Optical absorption of hemoglobin*, Tech. report, Oregon Medical Laser Center, Portland, U.S.A, 1999.

- [66] S.A. Prahl, *Light transport in tissue*, Ph.D. thesis, The University of Texas at Austin, TX, USA, December 1988.
- [67] S.A. Prahl, M. Keijzer, S.L. Jacques, and A.J. Welch, *A Monte Carlo model of light propagation in tissue*, SPIE Institute Series **IS 5** (1989), 102–111.
- [68] S.J. Preece and E. Claridge, *Monte carlo modelling of the spectral reflectance of the human eye*, Physics in Medicine and Biology **47** (2002), 2863–2877.
- [69] G. Prota, D. Hu, Maria R. Vincensi, S.A. McCormick, and A. Napolitano, *Characterization of melanins in human irides and cultured uveal melanocytes from eyes of different colors*, Experimental Eye Research **67** (1998), 293–299.
- [70] W. Purgathofer, *Open issues in photo-realistic rendering*, Computer Graphics Forum **22** (2003), no. 3, xix.
- [71] S. Regan, K.M. Egan, and E.S. Gragoudas, *Iris color as a risk factor in uveal melanoma*, Investigative Ophthalmology and Visual Science **38** (1997), no. 4, S810.
- [72] W. Rühle and A. Wild, *The intensification of absorbance changes in leaves by light-dispersion. differences between high-light and low-light leaves*, Planta **146** (1979), 551–557.
- [73] M.A. Sagar, D. Bullivant, G.D. Mallinson, P.J. Hunter, and I.W. Hunter, *A virtual environment and model of the eye for surgical simulation*, SIGGRAPH, Annual Conference Series (1994), 205–213.

- [74] F.W. Sears and M.W. Zemansky, *University physics, 3rd edition*, Addison-Wesley, Massachusetts, U.S.A., 1965.
- [75] J.M. Seddon, C.R. Sahagian, R.J. Glynn, R.D. Sperduto, E.S. Gragoudas, and the Eye Disorders Case-Control Study Group, *Evaluation of an iris color classification system*, Investigative Ophthalmology and Visual Science **31** (1990), no. 8, 1592–1598.
- [76] P. Shirley, *Physically based lighting for computer graphics*, Ph.D. thesis, Dept. of Computer Science, University of Illinois, November 1990.
- [77] R.S. Snell and M.A. Lemp, *Clinical anatomy of the eye*, Blackwell Scientific Publications, Massachusetts, U.S.A., 1989.
- [78] J. Stam, *An illumination model for a skin layer bounded by rough surfaces*, Rendering Techniques'2001 (Proceedings of the 12th Eurographics Rendering Workshop) (London) (P. M. Hanrahan and W. Purgathofer, eds.), Springer-Verlag, June 2001, pp. 39–52.
- [79] C.J. Stock, L.A. Canter, J.E. Puklin, and R.N. Frank, *Gender, race, iris color, and age-related macular degeneration*, Investigative Ophthalmology and Visual Science **36** (1995), no. 4, S10.
- [80] J.W. Strutt, *On the scattering of light by small particles*, Philosophical Magazine **41** (1871), no. 275, 447–454.

- [81] J.W. Strutt, *On the transmission of light through an atmosphere containing small particles in suspension, and on the origin of the blue of the sky*, Philosophical Magazine **47** (1899), 375–384.
- [82] T. Takamoto, B. Schwartz, L.B. Cantor, J.S. Hoop, and T. Steffens, *Measurement of iris color using computerized image analysis*, Current Eye Research **22** (2001), no. 6, 412–419.
- [83] M. Tsuchida, T. Miura, and K. Aibara, *Lipofuscin and lipofuscin-like substances*, Chemistry and Physics of Lipids **44** (1987), 297–325.
- [84] V. Tuchin, *Tissue optics: Light scattering methods and instruments for medical diagnosis, tutorial texts in optical engineering volume tt38*, SPIE - The International Society for Optical Engineering, Washington, U.S.A., 2000.
- [85] V.V. Tuchin, *Light scattering study of tissues*, Physics-Uspekhi **40** (1997), no. 5, 495–515.
- [86] J. Unander, *Project iris: Image reconstruction of the iris spectrally*, Tech. report, Munsell Color Science Laboratory, Rochester Institute of Technology, Rochester, U.S.A., 2000.
- [87] H.C. van de Hulst, *Multiple light scattering: Tables, formulas, and applications*, vol. 1, Academic Press, New York, U.S.A., 1980.
- [88] T.J.T.P. van den Berg and K.E.W.P. Tan, *Light transmittance of the human cornea from 320 to 700nm for different ages*, Vision Research **34** (1994), no. 11, 1453–1456.

- [89] D. van Norren and L.F. Tiemeijer, *Spectral reflectance of the human eye*, Vision Research **26** (1986), no. 2, 313–320.
- [90] T.C. Vogelmann, *Plant tissue optics*, Annual Review of Plant Physiology and Plant Molecular Biology **44** (1993), 231–251.
- [91] H. Wang, S. Lin, X. Liu, and S.B. Kang, *Separating reflections in human iris images for illumination estimation*, ICCV, 2005, pp. 1691–1698.
- [92] L. Wang, S.L. Jacques, and L. Zheng, *MCML – Monte Carlo modelling of light transport in multi-layered tissues*, Computer Methods and Programs in Biomedicine **47** (1995), 131–146.
- [93] A. Watt and M. Watt, *Advanced animation and rendering techniques*, Addison-Wesley, New York, 1992.
- [94] L. Wecker, F.Samavati, and M. Gavrilova, *Iris synthesis: A reverse subdivision technique*, 3rd International Conference on Computer Graphics and Interactive Techniques in Australasia and South East Asia (Dunedin, New Zealand), November 2005, pp. 121–125.
- [95] A. Wielgus and T. Sarna, *Photogeneration of superoxide anion by iris of the human eye under in vitro condition*, Current Topics in Biophysics **26** (2002), no. 1, 163–174.
- [96] R.P. Wildes, *Iris recognition: An emerging biometric technology*, Proceedings of IEEE **85** (1997), no. 9, 1348–1363.

- [97] C.L. Wilkerson, N.A. Syed, M.R. Fisher, N.L. Robinson, I.H.L. Wallow, and D.M. Albert, *Melanocytes and iris color, light microscopic findings*, Archives of Ophthalmology **114** (1996), 437–442.
- [98] B.C. Wilson and G. Adam, *A Monte Carlo model for the absorption and flux distributions of light in tissue*, Medical Physics **10** (1983), 824–830.
- [99] B. Winn, D. Whitaker, D.B. Elliott, and N.J. Phillips, *Factors affecting light-adapted pupil size in normal human subjects*, Investigative Ophthalmology & Visual Science **35** (1994), 1132–1137.
- [100] P.J. Wistrand, J. Stjernschantz, and K. Olsson, *The incidence and time-course of latanoprost-induced iridial pigmentation as a function of eye color*, Survey of Ophthalmology **41** (1997), S129–S138.
- [101] H.J. Wyatt and J. Ghosh, *Behaviour of an iris model and the pupil block hypothesis*, British Journal of Ophthalmology **54** (1970), 177–185.
- [102] G. Wyszecki and W.S. Stiles, *Color science, concepts and methods, quantitative data and formulae*, 2nd ed., John Wiley and Sons, Inc., New York, U.S.A., 1982.
- [103] F.P. Zscheile, J.W. White, B.W. Beadle, and J.R. Roach, *The preparation and absorption spectra of five pure carotenoid pigments*, Plant Physiology **17** (1942), no. 3, 331–346.

Index

- absorption, 3, 4, 19, 20
 - coefficient, 19–21
 - event, 13–15, 20, 22
 - model, 9
 - spectra, 10, 27, 31
- accuracy, 5, 23
- anterior border layer, 9, 10, 13, 15, 19,
24, 25, 29, 32, 33
- aqueous humor, 7, 8, 24
- attenuation, 20–22
- attenuation type, 22
- azimuthal angle, 15–16, 22
- backscatter, 8, 24
- blood
 - signature, 31
 - vessel, 11
- BRDF, 23, 33–34
- carotenoid, 10–12, 27
- chromatic
 - attribute, 2, 3, 9, 10, 32, 34, 40
 - variation, 9, 11, 33–35
- chromaticity, 3
- chromophore, 2
- collagen fibril, 9, 11, 21, 25
- colorimetry, 2
- connective tissue, 9
- cornea, 3, 7, 8, 24
- corneal polarization, 40
- cosine distribution, 15
- deoxyhemoglobin, 26
- diffuse, 11, 15–16
- environmental illumination, 3
- epithelial cell, 9
- eumelanic, 10
- eumelanin, 10, 19, 35
- eyeball, 7, 8
- factor of intensification, 27

- fibroblast, 9, 25
- Fresnel
 - coefficient, 15–16
 - equations, 15
 - test, 16
- geometrical optics, 13
- graphics hardware, 40
- hemoglobin, 10, 12, 26, 27, 31
 - deoxy, 10
 - oxy, 10
- image synthesis, 1, 4, 5, 40
- in vitro, 31
- in vivo, 24, 25, 27, 31, 63
- interface, 13, 15–19
- investigative ophthalmology, 3
- iridal
 - pattern, 3, 4, 34
 - pigmentation, 3, 9
- iris pigment epithelium, 9, 10, 13, 25
- lens, 7, 8
- light
 - distribution
 - spatial,, 23
 - spectral,, 23
 - interaction, 3–5, 7, 13, 15
 - propagation, 3, 4, 14, 16
 - transport, 4, 13, 20
- lipofuscin, 11
- lutein, 11, 27
- melanin, 10, 12, 26, 27, 29, 31–34
- Monte Carlo technique, 5, 40
- ocular
 - base material, 21, 25
 - degeneration, 3, 11
 - fundus, 3, 11
 - photoreceptor, 4
 - prosthetics, 4
 - tissue, 3, 7, 40
- oxyhemoglobin, 26
- phase function, 22
- pheomelanic, 10
- pheomelanin, 10, 19, 35
- pigment, 2, 9–11, 19, 26, 27, 29, 31, 63
- polar angle, 22
- predictability, 5, 23, 31, 32, 39

- predictive, 1, 4, 40
- pupil, 8, 10
 - radius, 26, 63
 - size, 3
- pupillary zone, 10
- qualitative, 5, 7, 10, 23, 29, 31, 33, 39
- quantitative, 5, 7, 10, 11, 24, 29–31, 39
- Rayleigh scattering, 11, 15, 20–22
- reflection, 3, 15, 24
 - specular, 59
- refraction, 15
- refractive index, 15, 21, 24, 25
- rejection sampling, 17, 18
- rendering, 1, 3–5, 40
- retina, 3
- scattering
 - coefficient, 20, 21
 - event, 14, 20, 22
- sclera, 7, 8, 34
- spectral
 - absorption coefficient, 12, 19
 - absorption curve, 27
 - characteristics, 10, 24
 - light distribution, 2
 - property, 26, 39
 - response, 29
 - shift, 31
 - signature, 2, 8, 9, 33, 34
- spectral response, 31
- stochastic
 - process, 13, 14
 - simulation, 40
- stromal layer, 9–11, 13, 15, 19, 20, 24–26, 29, 33
- surgical simulation, 3
- tear, 8, 24, 25, 40
- virtual
 - measurement device, 23, 60
 - specimen, 24, 26
- volume fraction, 21, 25
- warping function, 15
- wavelength dependence, 8, 24, 25
- zeaxanthin, 11, 27

Appendix A:

Directional Reflected Radiance

In the measurements performed by Imai [41] and Unander [86], the iridal specimen is uniformly illuminated from all directions by light with radiance $L_i(\lambda, d\omega_i)$, where $d\omega_i$ corresponds to the differential solid angle of the incident light. According to the radiative transfer theory [63], the hemispherical reflected radiance is given by:

$$L_r(\lambda, 2\pi) = \int_{\phi_i=0}^{\phi_i=2\pi} \int_{\theta_i=0}^{\theta_i=\pi/2} L_i(\lambda, d\omega_i) f_r(\lambda, d\omega_i, 2\pi) \cos \theta_i d\omega_i, \quad (6.1)$$

where $f_r(\lambda, d\omega_i, 2\pi)$ corresponds to specimen's directional-hemispherical BRDF.

Recall that a differential solid angle can be expressed as [63]:

$$d\omega = \sin \theta d\theta d\phi, \quad (6.2)$$

where the angles θ and ϕ correspond to the spherical coordinates of a sphere of unit radius.

Considering that the specular reflections were carefully excluded by Imai [41]

and Unander [86], and using the reflectance terminology and derivations provided by Nicodemus *et al.* [63], the specimen's directional-hemispherical BRDF can be approximated by:

$$f_r(\lambda, d\omega_i, 2\pi) = \frac{\rho(\lambda, d\omega_i, 2\pi)}{\pi}, \quad (6.3)$$

where $\rho(\lambda, d\omega_i, 2\pi)$ represents the directional-hemispherical reflectance (which is equal to the hemispherical-directional reflectance (radiance) factor [63]).

Plugging the BRDF expression given in Equation 6.3 into Equation 6.1, and solving the double integral, results in the following expression for the hemispherical reflected radiance:

$$L_r(\lambda, 2\pi) = L_i(\lambda, d\omega_i) \rho(\lambda, d\omega_i, 2\pi) \quad (6.4)$$

The directional reflected radiance can then be computed as [31]:

$$dL_r(\lambda, d\omega_r) = \frac{L_i(\lambda, d\omega_i) \rho(\lambda, d\omega_i, 2\pi)}{\int_{\phi_r=0}^{\phi_r=2\pi} \int_{\theta_r=0}^{\theta_r=\pi/2} \cos \theta_r d\omega_r}, \quad (6.5)$$

where $d\omega_r$ corresponds to the differential solid angle of the reflected light.

Solving the double integral in Equation 6.5, we get:

$$dL_r(\lambda, d\omega_r) = \frac{L_i(\lambda, d\omega_i) \rho(\lambda, d\omega_i, 2\pi)}{\pi}, \quad (6.6)$$

Considering a virtual spectrophotometer formulation [3],

the directional-hemispherical reflectance can be expressed as:

$$\rho(\lambda, d\omega_i, 2\pi) = \frac{m}{n}, \quad (6.7)$$

where m represents the number of rays reflected by the specimen and n represents the total number of rays shot towards the specimen, with each ray carrying the same amount of radiant power.

Replacing the directional-hemispherical reflectance in Equation 6.6 by the ratio given in Equation 6.7, results in the following expression for the directional reflected radiance:

$$dL_r(\lambda, d\omega_r) = \frac{L_i(\lambda, d\omega_i)}{\pi} \frac{m}{n}. \quad (6.8)$$

Appendix B:

Derivation of Pigment Concentrations

Considering the iris diameter to be $11mm$ [64, 96] with pupil radius of $2.5mm$ [64], the concentration, c , of a pigment with mass m can be approximated using the following expression:

$$c = m / ((h_A + h_S)(\pi((11mm/2)^2 - (2.5mm)^2))), \quad (6.9)$$

or simply,

$$c = m / ((h_A + h_S)(75.3982(mm^2))) \quad (6.10)$$

Due to the *in vivo* nature of the measurements made by Imai [41] and Unander [86], the concentrations of pigments used in Chapter 4 were obtained using average parameters provided in the biomedical literatures, namely eumelanin and

pheomelanin masses (represented by m_e and m_p respectively) from Prota *et al.*, [69], and lutein and zeaxanthin masses (represented by m_l and m_z respectively) from Berstein *et al.*, [7], these parameters are summarized in Table 6.1,

Table 6.1: Per-iris amount of pigments (μg).

Symbol	Value	Source
m_e	0 to 25.3	[69]
m_p	0.03 to 6.9	[69]
m_l	0.00403	[7]
m_z	0.00154	[7]

Appendix C:

Rendering Framework

All iris images of this thesis are rendered using a simple RGB Monte Carlo path tracing renderer [46] under a pure white light source with power of 800.0 units, which is selected to reasonably display the colour of the rendered iris with its low reflectivity without any clipping.

The correct conversion from a wavelength λ to RGB is a two-step process [33, 52]. Initially, one calculates the CIE tristimulus colour (X,Y,Z) using the spectral response $f(\lambda)$ and the CIE¹-1931 colour-matching functions $\bar{x}(\lambda)$, $\bar{y}(\lambda)$ and $\bar{z}(\lambda)$ [1]:

$$X = \int_{\lambda} f(\lambda) \bar{x}(\lambda) d\lambda \quad (6.11)$$

$$Y = \int_{\lambda} f(\lambda) \bar{y}(\lambda) d\lambda \quad (6.12)$$

$$Z = \int_{\lambda} f(\lambda) \bar{z}(\lambda) d\lambda \quad (6.13)$$

In practice, these integrals are often approximated by summations over m se-

¹Commission Internationale de L'Eclairage.

lected samples in the range of possible λ :

$$X = \sum_{i=1}^m f'_i \bar{x}_i \quad (6.14)$$

$$Y = \sum_{i=1}^m f'_i \bar{y}_i \quad (6.15)$$

$$Z = \sum_{i=1}^m f'_i \bar{z}_i \quad (6.16)$$

The corresponding RGB values are then obtained from transforming the XYZ values with a device-specific matrix [52, 33]:

$$\begin{bmatrix} R \\ G \\ B \end{bmatrix} = \begin{bmatrix} \text{device-} \\ \text{specific} \\ \text{transformation} \end{bmatrix} \begin{bmatrix} X \\ Y \\ Z \end{bmatrix} \quad (6.17)$$

Ideally, spectral information must be preserved for as long as possible in a rendering pipeline, and only converted to three dimensions (channels) when mapped to a specific device, such as a monitor or a printer, which may provide different colour solutions [5].

For the sake of simplicity, since we are not targeting a specific device, we choose three representative wavelengths (one for each colour channel) from the CIE-1931 chromaticity diagram, (650.0nm, 515.0nm, 475.0nm) to obtain the (R,G,B) values. These chromaticity coordinates were selected because their positions on diagram closely match the named colour patches "Red", "Green" and "Blue" [13].

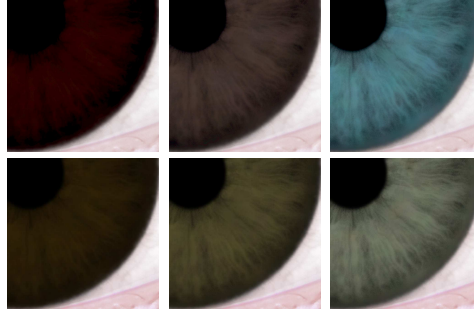


Figure 6.1: Images showing iridal chromatic variations obtained by varying the chromaticity coordinates. From left to right: (eumelanin concentration, pheomelanin concentration, ABL melanin portion) selected to be $(1.008mg/ml, 0.2674mg/ml, 80\%)$, $(0.4674mg/ml, 0.1124mg/ml, 50\%)$, and $(0.1201mg/ml, 0.0194mg/ml, 20\%)$ respectively. Top: using selected CIE-1931 chromaticity coordinates. Bottom: using SMPTE chromaticity coordinates.

Alternatively, SMPTE chromaticity coordinates² ($630.0nm, 557.7nm, 427.8nm$) can be used to derive the (R,G,B) values. Using these coordinates, one can obtain a higher tint of hazel and green (Figure 6.1).

²Society of Motion Picture and Television Engineers.

Appendix D:

Factor of Intensification

The actual path length involved in the simulation of an absorption event can vary due to two effects [90]:

1. Sieve effect: light passes through the medium without encountering an absorber. It reduces the medium's absorption efficiency.

2. Detour effect: light is scattered many times among the absorbers. It increases the medium's absorption efficiency.

Together, the sieve and the detour effects define a lengthening of the optical path length, or factor of intensification, which correlates to the concentration of an absorber in mg/m^2 [72], *i.e.*, the factor of intensification decreases with increasing pigment content.

The factor of intensification is taken into account in the ILIT model. However, since no data is available for melanin pigments, an approximation must be used.

Following the method of Appendix B, the concentration of eumelanin in the three iris samples (lightly-pigmented, moderately-pigmented and heavily-pigmented)

are calculated to be 0.1395mg/ml , 1.0192mg/ml and 1.2749mg/ml respectively - multiplying these concentrations by the thickness of the iris ($h_A + h_S = 0.34225\text{mm}$) accordingly gives concentrations of $4.77\mu\text{g/cm}^2$, $34.87\mu\text{g/cm}^2$ and $43.62\mu\text{g/cm}^2$.

The study of plant tissues by Rühle and Wild provides values for the factor of intensification for different chlorophyll concentrations (unit converted): 2.37 and 2.04 for $36.7\mu\text{g/cm}^2$ and $42.0\mu\text{g/cm}^2$ respectively [72]. By slightly extrapolating this range, it appears that a good value to use for the moderately-pigmented and the heavily-pigmented samples lies around 2.2.

Since no value is associated with a pigment concentration as low as the lightly-pigmented iris sample, and due to the opposite impact of lower pigment concentration on the sieve and detour effects, the same value of 2.2 is selected to minimize the introduction of bias in our comparisons.